



# Low-concentration CO<sub>2</sub> conversion on Ag<sub>x</sub>Na<sub>1-x</sub>TaO<sub>3</sub>-AgCl heterojunction photocatalyst

Qiaoqi Guo <sup>a,b</sup>, Ying Luo <sup>a,b</sup>, Jun Xu <sup>a,b</sup>, Lidan Deng <sup>c</sup>, Zheng Wang <sup>a,b,\*</sup>, Hong He <sup>a,b,\*</sup>

<sup>a</sup> State Key Joint Laboratory of Environment Simulation and Pollution Control, Research Center for Eco-Environmental Sciences, Chinese Academy of Sciences, Beijing 100085, China

<sup>b</sup> University of Chinese Academy of Sciences, Beijing 100049, China

<sup>c</sup> State Key Laboratory of Coal Combustion, School of Energy and Power Engineering, Huazhong University of Science and Technology, Wuhan 430074, China



## ARTICLE INFO

### Keywords:

Photocatalytic CO<sub>2</sub> conversion  
Low-concentration CO<sub>2</sub>  
Heterojunction structure  
Cation incorporation  
One-step flux synthesis

## ABSTRACT

Photocatalytic conversion of low-concentration CO<sub>2</sub> with H<sub>2</sub>O oxidation indicates an applicable way to achieve sustainable carbon cycling and solve the global warming problem. Enhancing photogenerated charge separation and surface adsorption and catalytic process of photocatalysts is the crucial point to compensate for the mass transfer limitation during low-concentration CO<sub>2</sub> conversion. Herein, a highly-crystalline Ag<sub>x</sub>Na<sub>1-x</sub>TaO<sub>3</sub>-AgCl heterostructure composite was successfully fabricated via a one-step flux method. The *in-situ* formation of intimate heterojunction between Ag<sub>x</sub>Na<sub>1-x</sub>TaO<sub>3</sub> and AgCl facilitated the separation and transfer of photogenerated charges. Moreover, the simultaneous introduction of Ag cations and AgCl components promoted the adsorption and activation of CO<sub>2</sub> on the photocatalyst surface. When combined with metallic Ag cocatalysts, the Ag<sub>x</sub>Na<sub>1-x</sub>TaO<sub>3</sub>-AgCl heterostructure photocatalyst exhibited an improved activity for the overall reaction of CO<sub>2</sub> reduction and H<sub>2</sub>O oxidation at low CO<sub>2</sub> concentration condition. The design of photocatalysts active at low CO<sub>2</sub> concentration accounts for an alternative way to construct the practical CO<sub>2</sub> conversion system in the future.

## 1. Introduction

The excessive emission of greenhouse gas CO<sub>2</sub> into the atmosphere has induced continuous global warming, resulting in remarkable climate change together with a series of critical eco-environmental issues [1–4]. The decrease of atmospheric CO<sub>2</sub> concentration and the removal of CO<sub>2</sub> gas from fossil fuel combustion based on carbon capture technologies can effectively prevent the deterioration of the eco-environment caused by the greenhouse effect [5–8]. From the viewpoint of carbon neutrality, it is significant and urgent to utilize CO<sub>2</sub> as a carbon resource to produce value-added fuels and chemicals upon CO<sub>2</sub> capture, which has drawn great attention in the fields of environment protection and energy conversion all over the world [9–11]. In this scenario, solar-driven CO<sub>2</sub> conversion on particulate photocatalysts has emerged as a promising strategy to simultaneously mitigate the increasing environmental problems and achieve sustainable carbon recycling [4,12–14].

Photocatalytic CO<sub>2</sub> conversion using H<sub>2</sub>O as the electron donor and proton source is a thermodynamically uphill reaction, which has been regarded as one of the simplest artificial photosynthetic ways towards

future practical application [15–17]. Over the past decades, tremendous efforts have been made to realize one-step excitation photocatalytic CO<sub>2</sub> conversion with H<sub>2</sub>O oxidation on ALA<sub>4</sub>Ti<sub>4</sub>O<sub>15</sub> (A = Ca, Sr, and Ba), Zn<sub>2</sub>GeO<sub>4</sub>, Ga<sub>2</sub>O<sub>3</sub>, ZnGa<sub>2</sub>O<sub>4</sub>, KCaSrTa<sub>5</sub>O<sub>15</sub>, NaTaO<sub>3</sub>, AgTaO<sub>3</sub>, et al [15, 18–23]. The feeding of high-concentration CO<sub>2</sub> gas into an alkaline solution is the necessary mass transfer condition to compensate for the limitation of charge separation and surface catalytic process for these photocatalysts. In consideration of energy depletion for CO<sub>2</sub> gas capture and purification, it is significantly important to investigate the photocatalytic conversion of low-concentration CO<sub>2</sub> with the oxidation of H<sub>2</sub>O [24,25]. Perovskite-type NaTaO<sub>3</sub> is a well-known photocatalyst for one-step excitation overall water splitting with the apparent quantum yield reaching 50% at 270 nm [26–28]. Because of its suitable band potential and high charge separation and transfer efficiency, NaTaO<sub>3</sub> has drawn extensive concern in photocatalytic overall reaction of CO<sub>2</sub> reduction and H<sub>2</sub>O oxidation [29–31]. Through the generation of surface active sites on NaTaO<sub>3</sub> photocatalyst by doping with Ca, Sr, Ba, or La ion, the photocatalytic activity for CO<sub>2</sub> reduction and H<sub>2</sub>O oxidation was dramatically enhanced in comparison with that of pristine NaTaO<sub>3</sub>.

\* Corresponding authors at: State Key Joint Laboratory of Environment Simulation and Pollution Control, Research Center for Eco-Environmental Sciences, Chinese Academy of Sciences, Beijing 100085, China

E-mail addresses: [zhengwang@rcees.ac.cn](mailto:zhengwang@rcees.ac.cn) (Z. Wang), [honghe@rcees.ac.cn](mailto:honghe@rcees.ac.cn) (H. He).

[9,22,29–34]. Moreover, the construction of heterojunction structure by combining  $\text{NaTaO}_3$  with  $\text{Ag}_3\text{PO}_4$ ,  $\text{Ag}_2\text{O}$  or  $\text{SrTiO}_3$  is also effective to decrease the recombination of electron-hole pairs, thereby markedly improving the photocatalytic performance [35–37].

In this work, we presented a facile approach for *in-situ* formation of  $\text{NaTaO}_3\text{-AgCl}$  heterostructure together with Ag cation incorporation into  $\text{NaTaO}_3$  by the one-step flux method. The suitable band alignment and the intimate interfacial junction of  $\text{Ag}_x\text{Na}_{1-x}\text{TaO}_3\text{-AgCl}$  composite facilitated the separation of photogenerated charges in the photocatalyst and its high crystallinity with decreased recombination centers promoted the charge carrier transfer efficiency. In addition, the simultaneous introduction of Ag cations and  $\text{AgCl}$  components provided sufficient active sites for  $\text{CO}_2$  adsorption to enhance the surface catalytic process. Owing to the synergistic effect, the  $\text{Ag}_x\text{Na}_{1-x}\text{TaO}_3\text{-AgCl}$  heterojunction photocatalyst modified with metallic Ag cocatalysts exhibited an impressive performance for the overall reaction of  $\text{CO}_2$  reduction and  $\text{H}_2\text{O}$  oxidation at low-concentration  $\text{CO}_2$  feeding condition.

## 2. Experimental section

### 2.1. Materials

$\text{Ag}_2\text{O}$  (99%, Innochem, China),  $\text{NaCl}$  (99%, Innochem, China),  $\text{Ta}_2\text{O}_5$  (99.99%, Aladdin, China),  $\text{Na}_2\text{CO}_3$  (99%, Sinopharm, China),  $\text{AgNO}_3$  (99%, Sinopharm, China),  $\text{NaPH}_2\text{O}_2$  (99.99%, Aladdin, China). All chemical reagents were used without further purification.

### 2.2. Synthesis

#### 2.2.1. Preparation of $\text{Ag}_x\text{Na}_{1-x}\text{TaO}_3\text{-AgCl}$ photocatalyst

$\text{Ag}_x\text{Na}_{1-x}\text{TaO}_3\text{-AgCl}$  photocatalyst was synthesized by the one-step flux method using  $\text{Ag}_2\text{O}$ ,  $\text{NaCl}$  and  $\text{Ta}_2\text{O}_5$  as starting materials. The starting materials were mixed in an agate mortar in a ratio of Na: Ta: Ag: Cl = 1: 2: 2: 1. Then excessive  $\text{NaCl}$  was added as flux. Typically, the solute concentration was defined as a molar ratio of  $\text{Ag}_x\text{Na}_{1-x}\text{TaO}_3\text{-AgCl}$  to that of the sum of  $\text{Ag}_x\text{Na}_{1-x}\text{TaO}_3\text{-AgCl}$  and the  $\text{NaCl}$  flux. The solute concentration was 10 mol%. The mixture was calcined in air at 1273 K for 15 h in an alumina crucible using a tube furnace. The calcined materials were washed with deionized water three times to remove the residual  $\text{NaCl}$  flux.

#### 2.2.2. Preparation of $\text{NaTaO}_3$ photocatalyst

$\text{NaTaO}_3$  was synthesized by the solid-state reaction method.  $\text{Na}_2\text{CO}_3$ ,  $\text{NaCl}$  and  $\text{Ta}_2\text{O}_5$  as starting materials were mixed in an agate mortar in a ratio of Na: Ta = 1: 1. And the ratio of  $\text{Na}_2\text{CO}_3$  and  $\text{NaCl}$  was 0.5: 1. The mixture was calcined in air at 1273 K for 15 h in an alumina crucible using a tube furnace.

#### 2.2.3. Preparation of $\text{Ag}_x\text{Na}_{1-x}\text{TaO}_3$ photocatalyst

$\text{Ag}_x\text{Na}_{1-x}\text{TaO}_3$  was synthesized by the solid-state reaction method.  $\text{Na}_2\text{CO}_3$ ,  $\text{Ta}_2\text{O}_5$ , and  $\text{Ag}_2\text{O}$  as starting materials were mixed in an agate mortar in a ratio of Na: Ta: Ag = 1.05: 2: 1. The mixture was calcined in air at 1273 K for 15 h in an alumina crucible using a tube furnace.

#### 2.2.4. Preparation of $\text{NaTaO}_3\text{-AgCl}$ photocatalyst

$\text{NaTaO}_3$  nanoparticles were synthesized by the solid-state reaction method. Then a certain amount (a ratio of Na: Ag = 1: 1) of  $\text{AgNO}_3$  aqueous solution was added to the beaker and finally added excessive amounts of  $\text{HCl}$  aqueous solution with magnetic stirring for 2 h. It was denoted as  $\text{NaTaO}_3\text{-AgCl}$ .

#### 2.2.5. Modification of photocatalyst with Ag cocatalyst

Ag cocatalyst was loaded by liquid-phase chemical reduction, impregnation, and photodeposition using  $\text{AgNO}_3$  as the precursors. In the liquid-phase chemical reduction method, an aqueous  $\text{AgNO}_3$  solution was added to a suspension containing the photocatalyst. After the

addition of aqueous  $\text{NaPH}_2\text{O}_2$  solution as a reducing reagent to the suspension, the mixture was stirred at 363 K for 2 h. The Ag-impregnated photocatalyst was reduced by  $\text{H}_2$  gas at 473 K for 1 h to obtain metallic Ag cocatalyst. The Ag cocatalyst was also loaded by *in-situ* photodeposition using  $\text{AgNO}_3$  as the precursors. For comparison, Ag-modified  $\text{Ag}_x\text{Na}_{1-x}\text{TaO}_3\text{-AgCl}$  composites with different loading amounts (1 wt%, 2 wt%, 3 wt%, 4 wt%, and 5 wt%) of Ag were prepared under identical conditions.

### 2.3. Characterization of photocatalysts

X-ray diffraction (XRD) was carried out using a Bruker, D8A A25 powder diffractometer equipped with a  $\text{Cu K}\alpha$  ( $\lambda = 0.154056$  nm) radiation source and using a voltage and current of 40 kV and 40 mA, respectively. X-ray photoelectron spectroscopy (XPS) measurement was implemented on a Thermo Scientific ESCALAB 250Xi spectrometer with a monochromatic  $\text{Al K}\alpha$  source ( $\hbar\nu = 1486.6$  eV) and normalized to C 1 s for each sample. Sputter-etching is performed using an ion beam with 4 keV  $\text{Ar}$  ions incident at an angle of 40°. The sputtering rates obtained using the reference  $\text{Ta}_2\text{O}_5$  sample are 0.82 nm/s. The area of the ion beam is over 1 mm<sup>2</sup>, while the area analyzed by XPS is 0.2 mm<sup>2</sup> and located in the center of the ion-etched region. Scanning electron microscopy images were taken using a field-emission scanning electron microscope (HITACHI, SU8020). High-resolution transmission electron microscope images were obtained using a JEM-2100Plus electron microscope operated at 200 kV. UV-vis diffuse reflectance spectroscopy (UV-vis DRS) was performed using a Perkin Elmer Lambda 650 S spectrometer equipped with an integrating sphere. A physisorption analyzer (Micromeritics, ASAP 2020 M) was used to obtain the specific surface area. The catalysts were degassed at 473 K for 6 h before measurement.

$\text{CO}_2$ -TPD experiments were carried out on a Nicolet IS50 spectrometer (Thermo, Beijing, China) with an MCT/A detector. Each sample (100 mg) with a quartz U-tube reactor was heated under ultra-high purity  $\text{N}_2$  flow (30 mL·min<sup>-1</sup>) up to 673 K at 283 K·min<sup>-1</sup> for 1 h and then it was cooled to room temperature. After pretreatment, 10%  $\text{CO}_2$  flow (total flow rate of  $\text{CO}_2$ / $\text{N}_2$  gases: 30 mL·min<sup>-1</sup>) passed through the catalyst bed for 30 min, subsequently, the sample was flushed by  $\text{N}_2$  flow (30 mL·min<sup>-1</sup>) for 60 min. Then, the TPD analysis was performed under  $\text{N}_2$  flow (30 mL·min<sup>-1</sup>) by heating the sample at a rate of 10 K·min<sup>-1</sup> up to 673 K. The calibration curve of the amount of  $\text{CO}_2$  was made by the decomposition of  $(\text{NH}_4)_2\text{CO}_3$  under the same testing conditions, and the amount of  $\text{CO}_2$  adsorbed on the sample was calculated based on this calibration curve.

### 2.4. Photoelectrochemical measurements

Electrochemical measurements were performed by using a CHI 650E electrochemical workstation with a standard three-electrode cell at room temperature. The prepared sample, an Ag/AgCl electrode (saturated KCl), and a Pt wire are used as the working electrode, the reference electrode, and the counter electrode, respectively. The preparation of working electrodes refers to the literature reported. A fluorine-doped tin oxide (FTO) glass piece with a size of 1 × 1 cm was sonicated in acetone and absolute ethanol, and then rinsed with deionized water and dried in an air stream. A suspension of 100 mg of the powder in 2 mL of absolute ethanol was used for casting onto the FTO glass substrate. The coated glass was then heated at 473 K in the air for 1 h to improve adhesion. The electrochemical impedance spectroscopy (EIS) was recorded by applying an AC voltage of 10 mV amplitude in the frequency range of 10<sup>5</sup> Hz to 10 Hz with the initial potential (0 V) in 0.1 M  $\text{Na}_2\text{SO}_4$ . For photocurrent measurement, a 300 W Xe arc lamp served as a light source and  $\text{Na}_2\text{SO}_4$  (0.1 M) aqueous solution was used as the electrolyte.

To estimate the conduction band potential ( $E_{\text{CB}}$ ), the flat-band potential ( $E_f$ ) of the samples was calculated by the Mott-Schottky equation. For n-type semiconductors,  $E_{\text{CB}} = E_f - 0.2$  V. Use the formula to

calculate the band gap ( $E_g$ ) =  $1240/\lambda g$  (eV). The valence band potential ( $E_{VB}$ ) can be calculated according to the following formula:  $E_{VB} = \varphi + E_{VB}$ , XPS - 4.44, where  $\varphi$  is the work function of the instrument (4.66 eV). Finally, the band gap relationship of different samples conforms to the empirical formula:  $E_g = E_{VB} - E_{CB}$ .

## 2.5. Photocatalytic $CO_2$ reduction test

Photocatalytic reactions were carried out in a gas-flow system using a top-irradiation cell equipped with a 300 W Xe lamp as a light source. The 0.3 g photocatalyst powder was dispersed in 100 mL of water. Ar gas (99.999%) was continuously introduced into the reactor before the reaction to remove the air. Photocatalytic reactions were carried out by flowing the  $CO_2$ /Ar mixed gas with a total rate of  $30 \text{ mL}\cdot\text{min}^{-1}$ . The concentration of  $CO_2$  in  $CO_2$ /Ar mixed gas was controlled by adjusting the flow rates of  $CO_2$  gas (99.9997%) and Ar gas (99.999%). The reaction system was connected to the cooling water system to maintain the reactor at room temperature. Gaseous products were determined by online gas chromatographs (Shimadzu, GC-2014) with a thermal conductivity detector (MS-13X, Ar carrier) and a flame ionization detector (SC-ST,  $N_2$  carrier) with a methanizer.

## 3. Results and discussion

### 3.1. Characterization of $Ag_xNa_{1-x}TaO_3$ -AgCl heterojunction photocatalyst

The crystal structure of  $Ag_xNa_{1-x}TaO_3$ -AgCl heterojunction photocatalyst was first analyzed. Fig. 1 shows XRD patterns of the obtained  $Ag_xNa_{1-x}TaO_3$ -AgCl,  $Ag_xNa_{1-x}TaO_3$ , NaTaO<sub>3</sub>-AgCl and NaTaO<sub>3</sub> samples. NaTaO<sub>3</sub> synthesized by the solid-state reaction method was pure phase according to the standard XRD pattern of JCPDS card No. 73-0878.  $Ag_xNa_{1-x}TaO_3$  sample exhibited the same XRD peaks of NaTaO<sub>3</sub> without any impurity phase, whereas  $Ag_xNa_{1-x}TaO_3$ -AgCl and NaTaO<sub>3</sub>-AgCl samples had the main phase of NaTaO<sub>3</sub> together with the appearance of typical XRD peaks corresponding to AgCl (JCPDS NO. 85-1355), suggesting the formation of heterostructure composite. The intensities of XRD peaks assigned to NaTaO<sub>3</sub> phase and AgCl phase in  $Ag_xNa_{1-x}TaO_3$ -AgCl composite were obviously higher than those in NaTaO<sub>3</sub> by solid-state reaction method and NaTaO<sub>3</sub>-AgCl with twofold AgCl weight ratio, indicating that highly-crystalline  $Ag_xNa_{1-x}TaO_3$ -AgCl composite was successfully grown in the one-step flux synthesis process. Moreover, the XRD peak positions of  $Ag_xNa_{1-x}TaO_3$ -AgCl and  $Ag_xNa_{1-x}TaO_3$  samples shifted to smaller diffraction angle as compared with pure NaTaO<sub>3</sub>, which implied Na<sup>+</sup> cations at the A sites of perovskite NaTaO<sub>3</sub> crystal structure were replaced by Ag<sup>+</sup> cations having the

slightly larger ionic radius. Considering the pure phase of the  $Ag_xNa_{1-x}TaO_3$  sample, the  $Ag_xNa_{1-x}TaO_3$  component in the  $Ag_xNa_{1-x}TaO_3$ -AgCl composite was a solid solution. As a result,  $Ag_xNa_{1-x}TaO_3$ -AgCl heterostructure photocatalyst with high crystallinity and homogeneous Ag incorporation was synthesized via the one-step flux method.

To investigate the chemical components from the surface to the interior of  $Ag_xNa_{1-x}TaO_3$ -AgCl, the depth analysis of XPS was carried out using Ar ion etching. Fig. 2 shows XPS spectra of the  $Ag_xNa_{1-x}TaO_3$ -AgCl composite acquired at the interval of Ar sputtering for 30.9 s and the elemental ratio at each step of Ar ion sputter-etching. The Ag 3d peaks of  $Ag_xNa_{1-x}TaO_3$ -AgCl in 61.8 s of Ar sputtering were mainly located at 373.1 and 367.1 eV (Fig. 2a), which were attributed to AgCl species. After Ar ion etching for 92.7 s, the locations of Ag 3d peaks shifted to 373.8 and 367.8 eV assigned to the binding energy between Ag cations and O anions, then were kept at the same position. In addition, the chemical states of Cl, Na, Ta, and O ions respectively remained unchanged (Fig. 2b-e). The elemental ratios from the surface to the interior of the  $Ag_xNa_{1-x}TaO_3$ -AgCl composite were estimated according to the areas of XPS peaks at each step of Ar sputtering. As shown in Fig. 2f, the amount of Cl element decreased with the increase of Ar etching time and was negligible after 92.7 s etching, related to the binding energy change of Ag element. Simultaneously, the concentrations of Ag, Na, Ta, and O ions in the  $Ag_xNa_{1-x}TaO_3$ -AgCl composite reached the steady ratio of 1: 1: 2: 6 after Ar sputtering for 92.7 s (Fig. 2f). Therefore, it is demonstrated that AgCl phase was grown on the surface of  $Ag_xNa_{1-x}TaO_3$  phase to form the intimate heterojunction in  $Ag_xNa_{1-x}TaO_3$ -AgCl composite and Ag cations were incorporated into NaTaO<sub>3</sub> structure as  $Ag_{0.5}Na_{0.5}TaO_3$ .

The morphology and interface structure of  $Ag_xNa_{1-x}TaO_3$ -AgCl heterojunction photocatalyst were investigated by SEM and TEM as shown in Fig. 3 and Fig. S1. In contrast to the cube-like shape of pristine NaTaO<sub>3</sub> with a clean surface (Fig. 3b),  $Ag_xNa_{1-x}TaO_3$ -AgCl composite by the one-step flux method exhibited the enlarged cuboid  $Ag_xNa_{1-x}TaO_3$  particles with the aggregated small AgCl grains on the surface (Fig. 3a), which agreed well with high crystallinity and heterostructure of  $Ag_xNa_{1-x}TaO_3$ -AgCl reflected from XRD and XPS results. Moreover, the HRTEM images of the  $Ag_xNa_{1-x}TaO_3$ -AgCl composite (Fig. S1) showed the clear lattice fringes related to  $Ag_xNa_{1-x}TaO_3$  and AgCl components and the intimate contact at the interface between the two phases. It is expected that the heterojunction structure in high-crystalline  $Ag_xNa_{1-x}TaO_3$ -AgCl photocatalyst will enable the efficient charge separation and migration to promote the conversion of  $CO_2$  in  $H_2O$ .

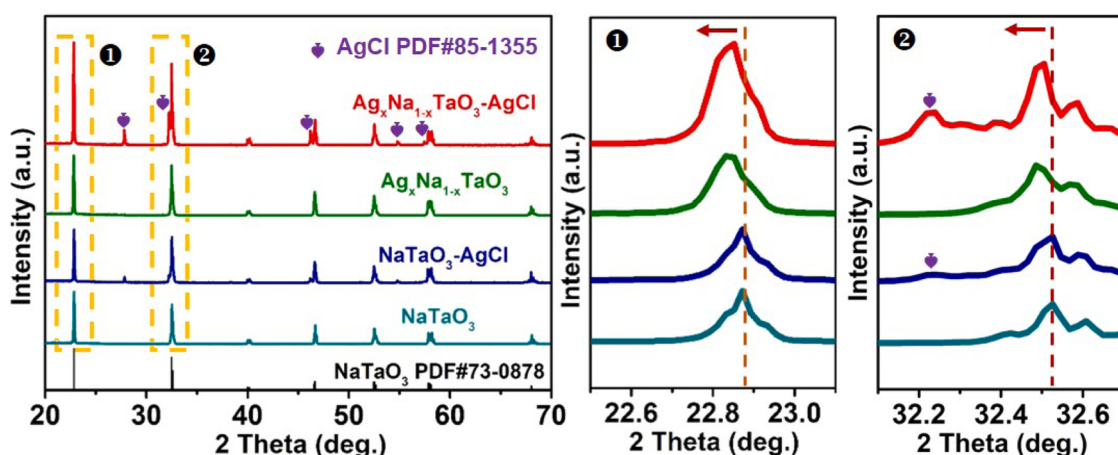


Fig. 1. XRD patterns of  $Ag_xNa_{1-x}TaO_3$ -AgCl,  $Ag_xNa_{1-x}TaO_3$ , NaTaO<sub>3</sub>-AgCl and NaTaO<sub>3</sub> samples.

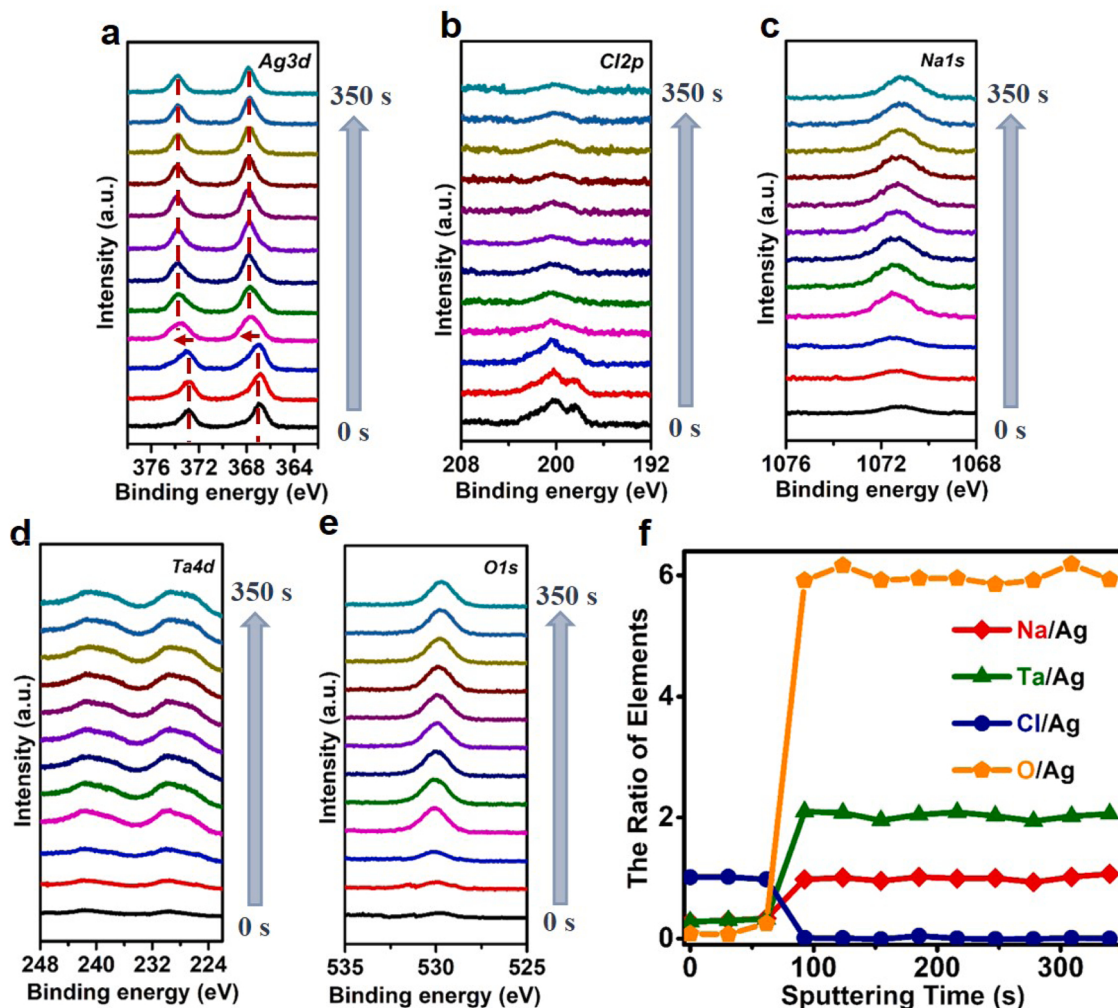


Fig. 2. XPS spectra of (a) Ag 3d, (b) Cl 2p, (c) Na 1 s, (d) Ta 4d, (e) O 1 s, and (f) the atomic ratio of each element for  $\text{Ag}_x\text{Na}_{1-x}\text{TaO}_3\text{-AgCl}$  during Ar ion etching.

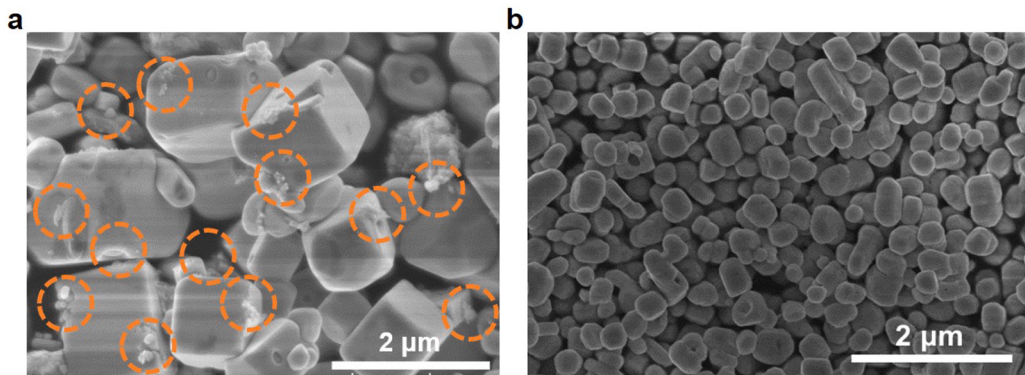
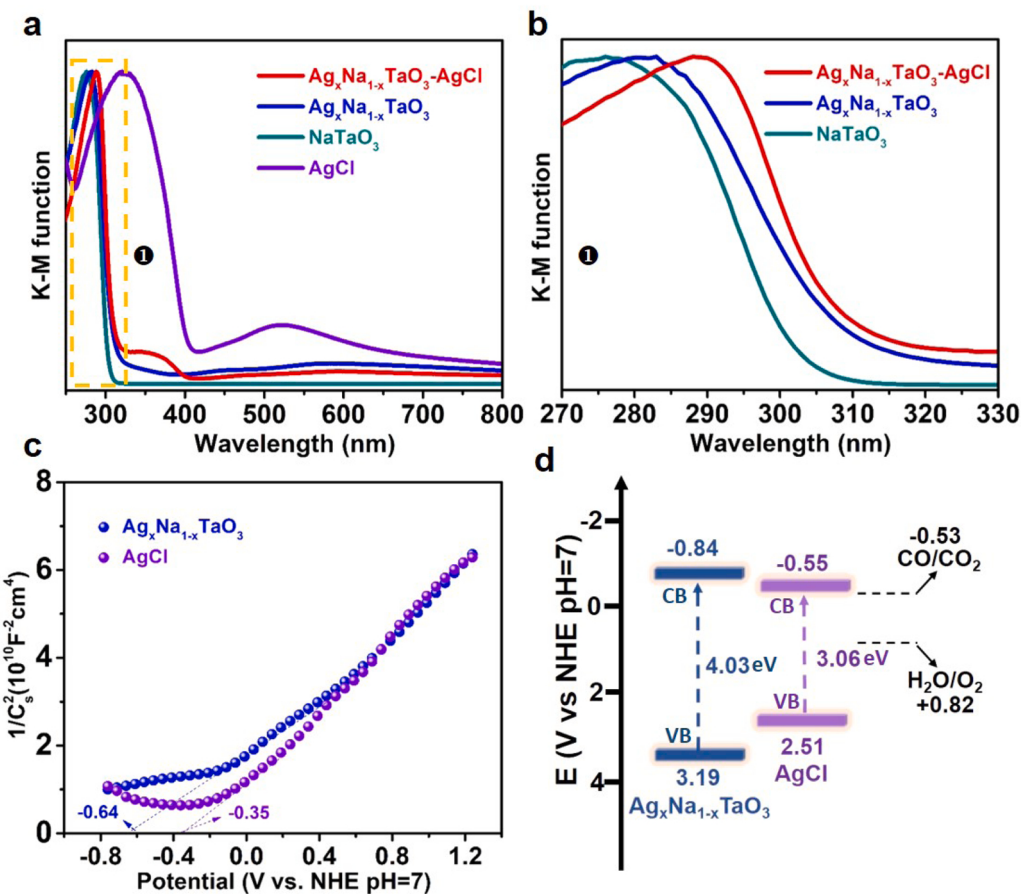


Fig. 3. SEM images of (a)  $\text{Ag}_x\text{Na}_{1-x}\text{TaO}_3\text{-AgCl}$  and (b) pristine  $\text{NaTaO}_3$  samples. The  $\text{Ag}_x\text{Na}_{1-x}\text{TaO}_3\text{-AgCl}$  was synthesized by the one-step flux method. The pristine  $\text{NaTaO}_3$  was synthesized by the solid-state reaction method.

### 3.2. Band structure and charge separation of $\text{Ag}_x\text{Na}_{1-x}\text{TaO}_3\text{-AgCl}$ photocatalyst

To further confirm the formation of heterojunction structure, the bandgap energy and band positions of  $\text{Ag}_x\text{Na}_{1-x}\text{TaO}_3$  and  $\text{AgCl}$  components in  $\text{Ag}_x\text{Na}_{1-x}\text{TaO}_3\text{-AgCl}$  were characterized by UV-vis DRS and Mott-Schottky plots. Fig. 4a-b display that the as-synthesized  $\text{NaTaO}_3$ ,  $\text{Ag}_x\text{Na}_{1-x}\text{TaO}_3$  and  $\text{AgCl}$  had the light absorption edges at 303 nm,

308 nm and 405 nm, corresponding to the band gap of 4.10 eV, 4.03 eV and 3.06 eV, respectively. Owing to the incorporation of Ag cations into the  $\text{NaTaO}_3$  matrix and the combination with  $\text{AgCl}$ , the  $\text{Ag}_x\text{Na}_{1-x}\text{TaO}_3\text{-AgCl}$  heterostructure photocatalyst exhibited a red shift of the absorption edge. The absorption background of  $\text{Ag}_x\text{Na}_{1-x}\text{TaO}_3\text{-AgCl}$  were higher than that of  $\text{NaTaO}_3$  due to the plasmon resonance effect of  $\text{AgCl}$  component and Ag incorporation. Moreover, the relative band potentials of  $\text{Ag}_x\text{Na}_{1-x}\text{TaO}_3$  and  $\text{AgCl}$  components in the  $\text{Ag}_x\text{Na}_{1-x}\text{TaO}_3\text{-AgCl}$



**Fig. 4.** (a-b) UV-vis DRS of  $\text{Ag}_x\text{Na}_{1-x}\text{TaO}_3$ -AgCl,  $\text{Ag}_x\text{Na}_{1-x}\text{TaO}_3$ ,  $\text{NaTaO}_3$  and AgCl, (c) Mott-Schottky plots of  $\text{Ag}_x\text{Na}_{1-x}\text{TaO}_3$  and AgCl, (d) the relative band positions of the  $\text{Ag}_x\text{Na}_{1-x}\text{TaO}_3$ -AgCl heterostructure.

composite were evaluated according to Mott-Schottky plots. In Fig. 4c, the flat-band potentials of  $\text{Ag}_x\text{Na}_{1-x}\text{TaO}_3$  and AgCl were fitted to be around  $-0.64$  V vs. NHE (pH 7), respectively. Considering that the bottom of the conduction band (CB) for n-type semiconductors (Mott-Schottky plots with positive slope) generally locates at about 0.2 V more negative potential than the flat band potential [38], the CB minimum positions of  $\text{Ag}_x\text{Na}_{1-x}\text{TaO}_3$  and AgCl were determined to be  $-0.84$  V and  $-0.55$  V, respectively. Moreover, the valence band (VB) maximum positions of  $\text{Ag}_x\text{Na}_{1-x}\text{TaO}_3$  and AgCl were acquired by XPS valence band spectra (Fig. S2), which is consistent with the estimation

from Mott-Schottky plots and the bandgap. In combination with these results, the band alignment of two components in  $\text{Ag}_x\text{Na}_{1-x}\text{TaO}_3$ -AgCl heterojunction photocatalyst was proposed in Fig. 4d. A typical type I heterojunction was formed in  $\text{Ag}_x\text{Na}_{1-x}\text{TaO}_3$ -AgCl photocatalyst, where CB and VB of  $\text{Ag}_x\text{Na}_{1-x}\text{TaO}_3$  component straddled those of AgCl component. Therefore, the transfer of photogenerated electrons from  $\text{Ag}_x\text{Na}_{1-x}\text{TaO}_3$  to AgCl in  $\text{Ag}_x\text{Na}_{1-x}\text{TaO}_3$ -AgCl heterojunction photocatalyst is thermodynamically feasible, leading to the efficient charge separation.

The effect of the heterojunction of  $\text{Ag}_x\text{Na}_{1-x}\text{TaO}_3$ -AgCl photocatalyst

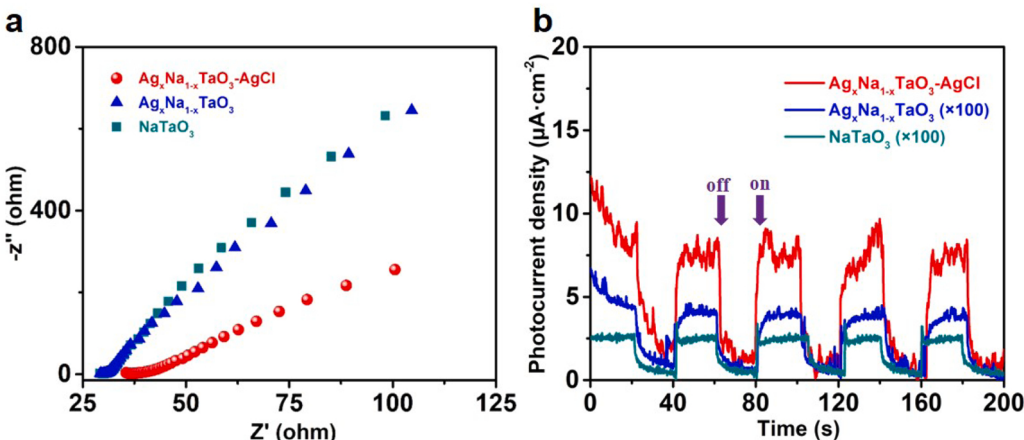


**Fig. 5.** (a) EIS Nyquist plots and (b) photocurrent density of  $\text{Ag}_x\text{Na}_{1-x}\text{TaO}_3$ -AgCl,  $\text{Ag}_x\text{Na}_{1-x}\text{TaO}_3$  and  $\text{NaTaO}_3$ .

on the separation efficiency of photogenerated electron-hole pairs was investigated by EIS and photocurrent measurements. Fig. 5a shows EIS Nyquist plots of  $\text{NaTaO}_3$ ,  $\text{Ag}_x\text{Na}_{1-x}\text{TaO}_3$  and  $\text{Ag}_x\text{Na}_{1-x}\text{TaO}_3\text{-AgCl}$  photocatalysts. As compared with pristine  $\text{NaTaO}_3$ , the slight decrease in the arc size of the EIS curve for  $\text{Ag}_x\text{Na}_{1-x}\text{TaO}_3$  photocatalyst indicates that Ag incorporation helped to reduce the charge-transfer resistance. Obviously, the  $\text{Ag}_x\text{Na}_{1-x}\text{TaO}_3\text{-AgCl}$  photocatalyst possessed the smallest resistance enabling fast separation and transfer of photogenerated charges. As a result, the photocurrent density of  $\text{Ag}_x\text{Na}_{1-x}\text{TaO}_3\text{-AgCl}$  was 145 times and 230 times higher than that of  $\text{Ag}_x\text{Na}_{1-x}\text{TaO}_3$  and  $\text{NaTaO}_3$  (Fig. 5b), respectively. The above results specifically confirm that efficient charge separation and transfer is readily available on the high-crystalline  $\text{Ag}_x\text{Na}_{1-x}\text{TaO}_3\text{-AgCl}$  heterojunction structure towards photocatalytic  $\text{CO}_2$  conversion with  $\text{H}_2\text{O}$  oxidation.

### 3.3. Photocatalytic conversion of low-concentration $\text{CO}_2$

In the photocatalytic  $\text{CO}_2$  reduction by  $\text{H}_2\text{O}$ , high-concentration  $\text{CO}_2$  gas is generally introduced into an alkaline solution for the improvement of  $\text{CO}_2$  solubility and  $\text{CO}_2$  mass transfer in the photocatalytic system [38–40]. To our knowledge, the production of high-concentration  $\text{CO}_2$  feedstock through the  $\text{CO}_2$  capture and purification process will demand more energy input for the practical application of  $\text{CO}_2$  conversion. Therefore, it is highly desirable to promote the performance for photocatalytic conversion of low-concentration  $\text{CO}_2$  with  $\text{H}_2\text{O}$  oxidation. The  $\text{CO}_2$  reduction reaction over the  $\text{Ag}_x\text{Na}_{1-x}\text{TaO}_3\text{-AgCl}$  heterojunction photocatalyst was carried out in pure  $\text{H}_2\text{O}$  with low-concentration  $\text{CO}_2$  flow under UV light irradiation. Fig. 6a shows the effect of different  $\text{CO}_2$  concentrations on the photocatalytic activity of  $\text{CO}_2$  conversion over bare  $\text{Ag}_x\text{Na}_{1-x}\text{TaO}_3\text{-AgCl}$ .  $\text{CO}$  gas as the reduction product and  $\text{O}_2$  gas as the oxidation product were simultaneously evolved, indicating that  $\text{H}_2\text{O}$  functioned as the electron donor for photocatalytic  $\text{CO}_2$  conversion. The selectivity towards  $\text{CO}_2$  reduction on the  $\text{Ag}_x\text{Na}_{1-x}\text{TaO}_3\text{-AgCl}$  photocatalyst was 100%. It is worth noting that the photocatalytic activity for  $\text{CO}_2$  reduction with  $\text{H}_2\text{O}$  oxidation gradually decreased with the increase of  $\text{CO}_2$  feeding concentration from 10% to 100%. It has been well-known that Ag cocatalyst can act as the active site for photocatalytic conversion of  $\text{CO}_2$  to produce  $\text{CO}$ , due to the moderate binding of Ag atom and  $\text{CO}$  molecule rendering smooth desorption of  $\text{CO}$  from Ag particle surface [41]. Therefore, when metallic Ag nanoparticles were uniformly dispersed on  $\text{Ag}_x\text{Na}_{1-x}\text{TaO}_3\text{-AgCl}$  which was confirmed by HRTEM and XPS (Fig. S3), the photocatalytic performance for  $\text{CO}_2$  reduction with  $\text{H}_2\text{O}$  oxidation over

the heterojunction photocatalyst was dramatically enhanced at various  $\text{CO}_2$  concentrations (Fig. 6b). The Ag-modified  $\text{Ag}_x\text{Na}_{1-x}\text{TaO}_3\text{-AgCl}$  photocatalyst exhibited superior activity at 10%  $\text{CO}_2$  feeding condition as well, and about 7.6 times higher evolution rate of  $\text{CO}$  than bare  $\text{Ag}_x\text{Na}_{1-x}\text{TaO}_3\text{-AgCl}$  photocatalyst. Additionally, the effects of the different loading methods and loading amounts of metallic Ag cocatalyst on the photocatalytic conversion of low-concentration  $\text{CO}_2$  were shown in Table S1. The optimal photocatalytic activity over  $\text{Ag}_x\text{Na}_{1-x}\text{TaO}_3\text{-AgCl}$  was obtained when 2 wt% metallic Ag cocatalyst was loaded by liquid-phase chemical reduction method. These results clearly demonstrate the validity of  $\text{Ag}_x\text{Na}_{1-x}\text{TaO}_3\text{-AgCl}$  heterojunction photocatalyst for the low-concentration  $\text{CO}_2$  conversion.

The activities of different  $\text{NaTaO}_3$ -based photocatalysts loaded with metallic Ag nanoparticulate cocatalyst at low-concentration  $\text{CO}_2$  were compared as shown in Fig. 7a-b. The evolution rates of  $\text{CO}$  from  $\text{CO}_2$  conversion on  $\text{NaTaO}_3\text{-AgCl}$  and  $\text{Ag}_x\text{Na}_{1-x}\text{TaO}_3$  photocatalysts were much higher than that on  $\text{NaTaO}_3$  photocatalyst, implying that the formation of heterostructure with  $\text{AgCl}$  and the incorporation of Ag into  $\text{NaTaO}_3$  crystal lattice both contributed to the activity enhancement. The optimal ratio between Na and Ag in  $\text{Ag}_x\text{Na}_{1-x}\text{TaO}_3$  solid solution (Table S2) was consistent with that in  $\text{Ag}_x\text{Na}_{1-x}\text{TaO}_3$  component of  $\text{Ag}_x\text{Na}_{1-x}\text{TaO}_3\text{-AgCl}$  heterostructure. The  $\text{Ag}_x\text{Na}_{1-x}\text{TaO}_3\text{-AgCl}$  heterojunction photocatalyst prepared via the high-temperature one-step flux method exhibited the increased crystallinity of  $\text{Ag}_x\text{Na}_{1-x}\text{TaO}_3$  and  $\text{AgCl}$  and the enhanced interfacial contact between these two components, so that the photocatalytic activity for low-concentration  $\text{CO}_2$  conversion was promoted to the level at least 20-fold higher than that of other three photocatalysts. Simultaneously,  $\text{O}_2$  was steadily evolved over Ag-modified  $\text{Ag}_x\text{Na}_{1-x}\text{TaO}_3\text{-AgCl}$  during photocatalytic  $\text{CO}_2$  conversion as shown in Fig. S4, and Ag-modified  $\text{Ag}_x\text{Na}_{1-x}\text{TaO}_3\text{-AgCl}$  photocatalyst was unchangeable before and after  $\text{CO}_2$  conversion reaction confirmed by SEM images and XRD patterns (Fig. S5). Furthermore, the photocatalytic  $\text{CO}_2$  reduction performance correlated well with the  $\text{CO}_2$  adsorption capacities of four photocatalysts, increased in the order of  $\text{NaTaO}_3$ ,  $\text{Ag}_x\text{Na}_{1-x}\text{TaO}_3$ ,  $\text{NaTaO}_3\text{-AgCl}$  and  $\text{Ag}_x\text{Na}_{1-x}\text{TaO}_3\text{-AgCl}$  regardless of the similar specific surface areas (Fig. 7c and Table S3-4). As a result, the high-crystalline  $\text{Ag}_x\text{Na}_{1-x}\text{TaO}_3\text{-AgCl}$  heterojunction structure afforded the fast separation and transfer of photogenerated charges, and the combination of  $\text{Ag}_x\text{Na}_{1-x}\text{TaO}_3$  and  $\text{AgCl}$  components allowed the strengthened chemisorption and activation of  $\text{CO}_2$  molecules. Both of these two aspects integrally overcame the condition of low mass transfer and exchange, thus facilitating the photocatalytic conversion of low-concentration  $\text{CO}_2$  with  $\text{H}_2\text{O}$  oxidation over

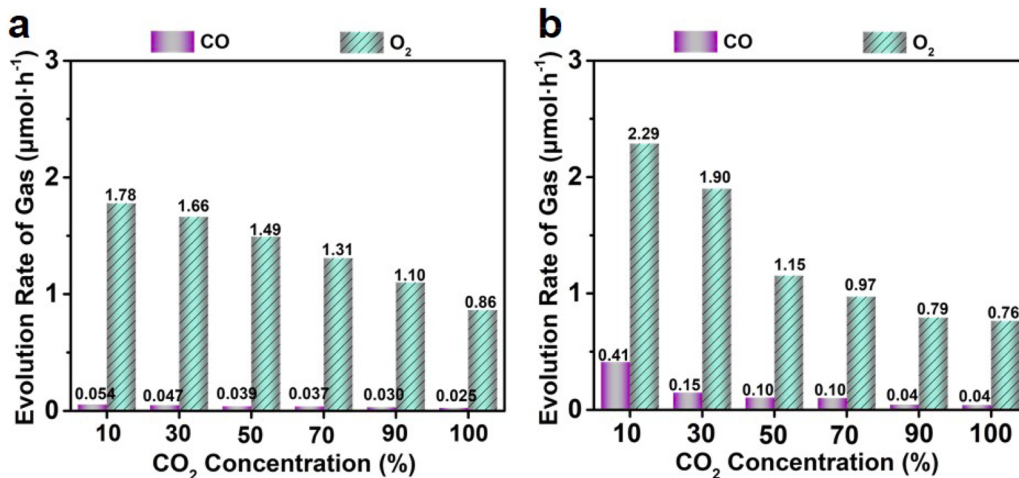
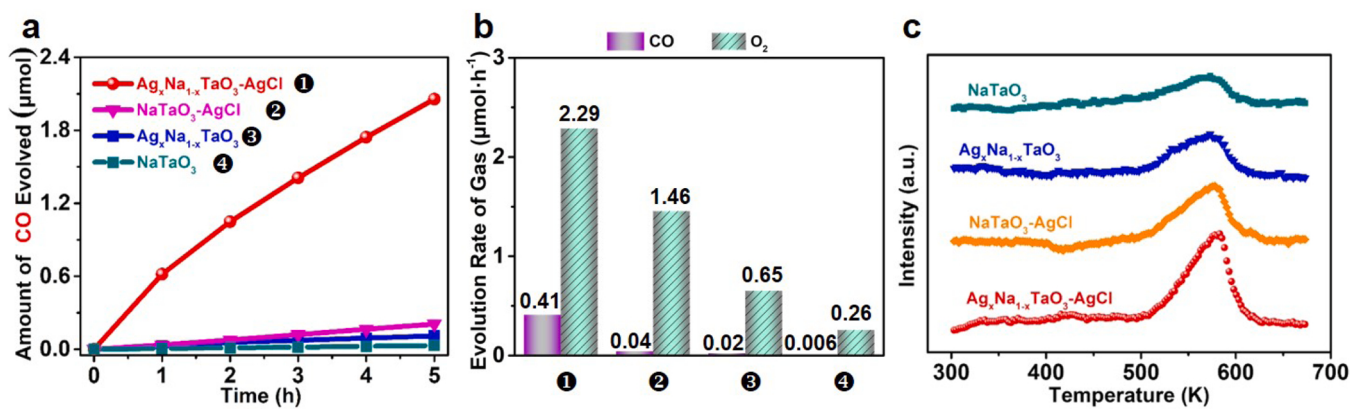


Fig. 6. Evolution rates of CO and  $\text{O}_2$  over (a) bare  $\text{Ag}_x\text{Na}_{1-x}\text{TaO}_3\text{-AgCl}$  photocatalyst and (b) Ag-modified  $\text{Ag}_x\text{Na}_{1-x}\text{TaO}_3\text{-AgCl}$  photocatalyst at different  $\text{CO}_2$  concentrations; Photocatalyst: 0.3 g; cocatalyst: 2 wt% of Ag by a liquid phase reduction method; reactant solution: 100 mL pure water;  $\text{CO}_2\text{/Ar}$  gas flow rate: 30  $\text{mL}\cdot\text{min}^{-1}$ ; light

Source: 300 W Xe-lamp.



**Fig. 7.** (a) The amount of CO evolution and (b) Evolution rate of CO and  $\text{O}_2$  over Ag-modified  $\text{Ag}_x\text{Na}_{1-x}\text{TaO}_3\text{-AgCl}$ , Ag-modified  $\text{NaTaO}_3\text{-AgCl}$ , Ag-modified  $\text{Ag}_x\text{Na}_{1-x}\text{TaO}_3$  and Ag-modified  $\text{NaTaO}_3$  at 10%  $\text{CO}_2$  concentration. Photocatalyst: 0.3 g; cocatalyst: 2 wt% of Ag by a liquid phase reduction method; reactant solution: 100 mL pure water;  $\text{CO}_2/\text{Ar}$  gas flow rate: 30  $\text{mL}\cdot\text{min}^{-1}$ ; light source: 300 W Xe-lamp; (c)  $\text{CO}_2$ -TPD profiles for  $\text{Ag}_x\text{Na}_{1-x}\text{TaO}_3\text{-AgCl}$ ,  $\text{NaTaO}_3\text{-AgCl}$ ,  $\text{Ag}_x\text{Na}_{1-x}\text{TaO}_3$  and  $\text{NaTaO}_3$  samples.

$\text{Ag}_x\text{Na}_{1-x}\text{TaO}_3\text{-AgCl}$  photocatalyst. In addition, most of photocatalysts for low-concentration  $\text{CO}_2$  conversion in the literatures (Table S5) were either synthesized in a complicated process or functioned in the system containing sacrificial reagent. Our  $\text{Ag}_x\text{Na}_{1-x}\text{TaO}_3\text{-AgCl}$  heterojunction photocatalyst fabricated by a facile one-step flux method had the advantages in low-concentration  $\text{CO}_2$  conversion using  $\text{H}_2\text{O}$  as electron donor. Nevertheless, the conversion efficiency of low-concentration  $\text{CO}_2$  on  $\text{Ag}_x\text{Na}_{1-x}\text{TaO}_3\text{-AgCl}$  heterojunction photocatalyst are necessary to be further improved.

#### 4. Conclusion

The  $\text{Ag}_x\text{Na}_{1-x}\text{TaO}_3\text{-AgCl}$  photocatalyst with the high-crystalline heterojunction structure has been successfully fabricated via a one-step flux method. The *in-situ* combination of  $\text{Ag}_x\text{Na}_{1-x}\text{TaO}_3$  and  $\text{AgCl}$  components at high temperature made a strong interaction at the junction interface, so the matched band positions and the decreased recombination centers in  $\text{Ag}_x\text{Na}_{1-x}\text{TaO}_3\text{-AgCl}$  heterostructure encouraged the separation and transfer efficiency of photogenerated electron-hole pairs. In addition, the presence of surface Ag cations in  $\text{Ag}_x\text{Na}_{1-x}\text{TaO}_3$  and  $\text{AgCl}$  particles on  $\text{Ag}_x\text{Na}_{1-x}\text{TaO}_3$  greatly enforced  $\text{CO}_2$  adsorption capability. Upon the modification with metallic Ag nanoparticles as the active reduction cocatalyst, the high-crystalline  $\text{Ag}_x\text{Na}_{1-x}\text{TaO}_3\text{-AgCl}$  heterostructure gave the remarkably improved photocatalytic activity for the conversion of low-concentration  $\text{CO}_2$  with  $\text{H}_2\text{O}$  oxidation. Accordingly, this study provided an effective method for the development of heterojunction photocatalysts achieving efficient solar-to-chemical energy conversion.

#### CRediT authorship contribution statement

**Qiaochi Guo:** Investigation, Formal analysis, Data curation, Writing - original draft, Writing – review & editing. **Ying Luo:** Investigation, Formal analysis, Data curation, Methodology, Validation. **Jun Xu:** Formal analysis, Data curation, Methodology, Writing – review & editing. **Lidan Deng:** Writing - review & editing, Validation. **Zheng Wang:** Conceptualization, Methodology, Validation, Writing – review & editing, Project administration, Resources, Supervision. **Hong He:** Conceptualization, Writing – review & editing, Project administration, Resources, Supervision.

#### Declaration of Competing Interest

The authors declare that they have no known competing financial interests or personal relationships that could have appeared to influence

the work reported in this paper.

#### Data availability

Data will be made available on request.

#### Acknowledgments

This work was financially supported by the Pioneer Initiative Action Project of Chinese Academy of Sciences, the Youth Talent Scholars and the Young Scientists Fund of National Natural Science Foundation of China and the Program for Science and Technology Innovation Talents in Universities of Henan Province.

#### Appendix A. Supporting information

Supplementary data associated with this article can be found in the online version at doi:10.1016/j.apcatb.2022.122253.

#### References

- [1] A.A. Lacis, G.A. Schmidt, D. Rind, R.A. Ruedy, Atmospheric  $\text{CO}_2$ : principal control knob governing earth's temperature, *Science* 330 (2010) 356–359.
- [2] W.R. Peltier, A. Tushingham, Global sea level rise and the greenhouse effect: might they be connected? *Science* 244 (1989) 806–810.
- [3] Y. He, L. Zhang, B. Teng, M. Fan, New application of Z-scheme  $\text{Ag}_3\text{PO}_4/\text{g-C}_3\text{N}_4$  composite in converting  $\text{CO}_2$  to fuel, *Environ. Sci. Technol.* 49 (2015) 649–656.
- [4] W. Zhang, D. Ma, J. Pérez-Ramírez, Z. Chen, Recent progress in materials exploration for thermocatalytic, photocatalytic, and integrated photothermocatalytic  $\text{CO}_2$ -to-fuel conversion, *Adv. Energy Sustain. Res.* 3 (2022), 2100169.
- [5] T. Wilberforce, A. Olabi, E.T. Sayed, K. Elsaied, M.A. Abdelkareem, Progress in carbon capture technologies, *Sci. Total Environ.* 761 (2021), 143203.
- [6] P. Markewitz, W. Kuckshinrichs, W. Leitner, J. Linssen, P. Zapp, R. Bongartz, A. Schreiber, T.E. Müller, Worldwide innovations in the development of carbon capture technologies and the utilization of  $\text{CO}_2$ , *Energy Environ. Sci.* 5 (2012) 7281–7305.
- [7] Y.H. Yan, T. Borhani, G. Subraveti, N. Pai, V. Prasad, A. Rajendran, P. Nkulikiyinka, J.O. Asibor, Z. Zhang, D. Shao, Harnessing the power of machine learning for carbon capture, utilisation, and storage (CCUS)-a state-of-the-art review, *Energy Environ. Sci.* 14 (2021) 6122–6157.
- [8] Z. Zhang, T. Wang, M.J. Blunt, E.J. Anthony, A.-H.A. Park, R.W. Hughes, P. A. Webley, J. Yan, Advances in carbon capture, utilization and storage, *Appl. Energy* 278 (2020), 115627.
- [9] G. Zhang, G. Liu, L. Wang, J.T. Irvine, Inorganic perovskite photocatalysts for solar energy utilization, *Chem. Soc. Rev.* 45 (2016) 5951–5984.
- [10] J. Ran, M. Jaroniec, S.Z. Qiao, Cocatalysts in semiconductor-based photocatalytic  $\text{CO}_2$  reduction: achievements, challenges, and opportunities, *Adv. Mater.* 30 (2018), 1704649.
- [11] H. Wang, L. Zhang, Z. Chen, J. Hu, S. Li, Z. Wang, J. Liu, X. Wang, Semiconductor heterojunction photocatalysts: design, construction, and photocatalytic performances, *Chem. Soc. Rev.* 43 (2014) 5234–5244.

[12] J.L. DiMeglio, J. Rosenthal, Selective conversion of CO<sub>2</sub> to CO with high efficiency using an inexpensive bismuth-based electrocatalyst, *J. Am. Chem. Soc.* 135 (2013) 8798–8801.

[13] Y. Chen, C.W. Li, M.W. Kanan, Aqueous CO<sub>2</sub> reduction at very low overpotential on oxide-derived Au nanoparticles, *J. Am. Chem. Soc.* 134 (2012) 19969–19972.

[14] S. Cao, B. Shen, T. Tong, J. Fu, J. Yu, 2D/2D heterojunction of ultrathin MXene/Bi<sub>2</sub>WO<sub>6</sub> nanosheets for improved photocatalytic CO<sub>2</sub> reduction, *Adv. Funct. Mater.* 28 (2018) 1800136.

[15] Z. Wang, K. Teramura, S. Hosokawa, T. Tanaka, Highly efficient photocatalytic conversion of CO<sub>2</sub> into solid CO using H<sub>2</sub>O as a reductant over Ag-modified ZnGa<sub>2</sub>O<sub>4</sub>, *J. Mater. Chem. A* 3 (2015) 11313–11319.

[16] Z. Wang, K. Teramura, S. Hosokawa, T. Tanaka, Photocatalytic conversion of CO<sub>2</sub> in water over Ag-modified La<sub>2</sub>Ti<sub>2</sub>O<sub>7</sub>, *Appl. Catal. B Environ.* 163 (2015) 241–247.

[17] S. Yan, J. Wang, H. Gao, N. Wang, H. Yu, Z. Li, Y. Zhou, Z. Zou, Zinc gallogermanate solid solution: a novel photocatalyst for efficiently converting CO<sub>2</sub> into solar fuels, *Adv. Funct. Mater.* 23 (2013) 1839–1845.

[18] K. Iizuka, T. Wato, Y. Miseki, K. Saito, A. Kudo, Photocatalytic reduction of carbon dioxide over Ag cocatalyst-loaded Al<sub>0.4</sub>Ti<sub>0.15</sub>O<sub>15</sub> (A= Ca, Sr, and Ba) using water as a reducing reagent, *J. Am. Chem. Soc.* 133 (2011) 20863–20868.

[19] S. Yan, L. Wan, Z. Li, Z. Zou, Facile temperature-controlled synthesis of hexagonal Zn<sub>2</sub>GeO<sub>4</sub> nanorods with different aspect ratios toward improved photocatalytic activity for overall water splitting and photoreduction of CO<sub>2</sub>, *Chem. Commun.* 47 (2011) 5632–5634.

[20] R. Ito, M. Akatsuka, A. Ozawa, Y. Kato, Y. Kawaguchi, M. Yamamoto, T. Tanabe, T. Yoshida, Photocatalytic activity of Ga<sub>2</sub>O<sub>3</sub> supported on Al<sub>2</sub>O<sub>3</sub> for water splitting and CO<sub>2</sub> reduction, *ACS Omega* 4 (2019) 5451–5458.

[21] T. Takayama, A. Iwase, A. Kudo, Photocatalytic water splitting and CO<sub>2</sub> reduction over KCaSrTa<sub>5</sub>O<sub>15</sub> nanorod prepared by a polymerized complex method, *Bull. Chem. Soc. Jpn.* 88 (2015) 538–543.

[22] H. Nakanishi, K. Iizuka, T. Takayama, A. Iwase, A. Kudo, Highly active NaTaO<sub>3</sub>-based photocatalysts for CO<sub>2</sub> reduction to form CO using water as the electron donor, *ChemSusChem* 10 (2017) 112–118.

[23] Q. Guo, J. Xu, Y. Luo, Y. Yang, Z. Wang, H. He, Cocatalyst modification of AgTaO<sub>3</sub> photocatalyst for conversion of carbon dioxide with water, *J. Phys. Chem. C* 125 (2021) 26389–26397.

[24] X. Wu, Y. Li, G. Zhang, H. Chen, J. Li, K. Wang, Y. Pan, Y. Zhao, Y. Sun, Y. Xie, Photocatalytic CO<sub>2</sub> conversion of M<sub>0.33</sub>WO<sub>3</sub> directly from the air with high selectivity: insight into full spectrum-induced reaction mechanism, *J. Am. Chem. Soc.* 141 (2019) 5267–5274.

[25] S. You, S. Guo, X. Zhao, M. Sun, C. Sun, Z. Su, X. Wang, All-inorganic perovskite/graphitic carbon nitride composites for CO<sub>2</sub> photoreduction into C1 compounds under low concentrations of CO<sub>2</sub>, *Dalton Trans.* 48 (2019) 14115–14121.

[26] Z. Wang, C. Li, K. Domen, Recent developments in heterogeneous photocatalysts for solar-driven overall water splitting, *Chem. Soc. Rev.* 48 (2019) 2109–2125.

[27] E. Grabowska, Selected perovskite oxides: characterization, preparation and photocatalytic properties-a review, *Appl. Catal. B Environ.* 186 (2016) 97–126.

[28] H. Kato, K. Asakura, A. Kudo, Highly efficient water splitting into H<sub>2</sub> and O<sub>2</sub> over lanthanum-doped NaTaO<sub>3</sub> photocatalysts with high crystallinity and surface nanostructure, *J. Am. Chem. Soc.* 125 (2003) 3082–3089.

[29] G.R. Portugal, S.F. Santos, J.T. Arantes, NaTaO<sub>3</sub> cubic and orthorhombic surfaces: an intrinsic improvement of photocatalytic properties, *Appl. Surf. Sci.* 502 (2020) 144206.

[30] V. Jeyalakshmi, R. Mahalakshmy, K. Ramesh, P.V. Rao, N.V. Choudary, K. Thirunavukkarasu, K.R. Krishnamurthy, B. Viswanathan, Metal oxides as photocatalysts: modified sodium tantalate as catalyst for photoreduction of carbon dioxide, *Mol. Catal.* 451 (2018) 105–113.

[31] L. An, H. Onishi, Electron-hole recombination controlled by metal doping sites in NaTaO<sub>3</sub> photocatalysts, *ACS Catal.* 5 (2015) 3196–3206.

[32] H. Sudrajat, S. Babel, I. Thushari, K. Laohhasurayotin, Stability of La dopants in NaTaO<sub>3</sub> photocatalysts, *J. Alloy. Compd.* 775 (2019) 1277–1285.

[33] H. Li, X. Shi, X. Liu, X. Li, Synthesis of novel, visible-light driven S, N-doped NaTaO<sub>3</sub> catalysts with high photocatalytic activity, *Appl. Surf. Sci.* 508 (2020), 145306.

[34] J. Mora-Hernandez, A.M. Huerta-Flores, L.M. Torres-Martinez, Photoelectrocatalytic characterization of carbon-doped NaTaO<sub>3</sub> applied in the photoreduction of CO<sub>2</sub> towards the formaldehyde production, *J. CO<sub>2</sub> Util.* 27 (2018) 179–187.

[35] X. Wang, J. Ma, Y. Kong, C. Fan, M. Peng, S. Komarneni, Synthesis of p-n heterojunction Ag<sub>3</sub>PO<sub>4</sub>/NaTaO<sub>3</sub> composite photocatalyst for enhanced visible-light-driven photocatalytic performance, *Mater. Lett.* 251 (2019) 192–195.

[36] S. Yang, D. Xu, B. Chen, B. Luo, X. Yan, L. Xiao, W. Shi, Synthesis and visible-light-driven photocatalytic activity of p-n heterojunction Ag<sub>2</sub>O/NaTaO<sub>3</sub> nanocubes, *Appl. Surf. Sci.* 383 (2016) 214–221.

[37] G.Z. Wang, H. Chen, X.K. Luo, H.K. Yuan, A.L. Kuang, Bandgap engineering of SrTiO<sub>3</sub>/NaTaO<sub>3</sub> heterojunction for visible light photocatalysis, *Int. J. Quantum Chem.* 117 (2017), e25424.

[38] Y. Qi, S. Chen, M. Li, Q. Ding, Z. Li, J. Cui, B. Dong, F. Zhang, C. Li, Achievement of visible-light-driven Z-scheme overall water splitting using barium-modified Ta<sub>3</sub>N<sub>5</sub> as a H<sub>2</sub>-evolving photocatalyst, *Chem. Sci.* 8 (2017) 437–443.

[39] S. Wang, K. Teramura, T. Hisatomi, K. Domen, H. Asakura, S. Hosokawa, T. Tanaka, Effective driving of Ag-loaded and Al-doped SrTiO<sub>3</sub> under irradiation at  $\lambda > 300$  nm for the photocatalytic conversion of CO<sub>2</sub> by H<sub>2</sub>O, *ACS Appl. Energy Mater.* 3 (2020) 1468–1475.

[40] R. Pang, K. Teramura, H. Asakura, S. Hosokawa, T. Tanaka, Effect of Cr species on photocatalytic stability during the conversion of CO<sub>2</sub> by H<sub>2</sub>O, *J. Phys. Chem. C* 123 (2019) 2894–2899.

[41] M. Yamamoto, T. Yoshida, N. Yamamoto, T. Nomoto, Y. Yamamoto, S. Yagi, H. Yoshida, Photocatalytic reduction of CO<sub>2</sub> with water promoted by Ag clusters in Ag/Ga<sub>2</sub>O<sub>3</sub> photocatalysts, *J. Mater. Chem. A* 3 (2015) 16810–16816.